





Thermoelectric phenomena in an antiferromagnetic helix: Role of electric fieldKallol Mondal ^{1,2,*} Sudin Ganguly ^{3,†} and Santanu K. Maiti ^{4,‡}¹*School of Physical Sciences, National Institute of Science Education and Research Bhubaneswar, Jatni, Odisha 752050, India*²*Homi Bhabha National Institute, Training School Complex, Anushaktinagar, Mumbai 400094, India*³*Department of Physics, School of Applied Sciences, University of Science and Technology Meghalaya, Ri-Bhoi-793101, India*⁴*Physics and Applied Mathematics Unit, Indian Statistical Institute, 203 Barrackpore Trunk Road, Kolkata-700108, India* (Received 16 May 2023; revised 5 October 2023; accepted 17 October 2023; published 1 November 2023)

The charge and spin-dependent thermoelectric responses are investigated on a single-stranded helical system possessing a collinear antiferromagnetic spin arrangement with zero net magnetization in the presence of a transverse electric field. Both the short and long-range hopping scenarios are considered. Nonequilibrium Green's function formalism is employed following the Landauer-Buttiker prescription to study the thermoelectric phenomena. The dependence of the thermoelectric quantities on electric field, temperature, parameters associated with the helical geometry, coupling of the helix to electrodes, system size, etc., are elaborately discussed. The charge and spin *figure of merits* are computed and compared critically. For a more accurate estimation, the phononic contribution towards thermal conductance is also included. The present proposition shows a favorable spin-dependent thermoelectric response compared to the charge counterpart.

DOI: [10.1103/PhysRevB.108.195401](https://doi.org/10.1103/PhysRevB.108.195401)**I. INTRODUCTION**

Achieving a favorable thermoelectric (TE) response is a long-sought goal in the material science community to overcome the dilemma of the global energy crisis. This is due to the fact that heat-to-energy conversion potentially can be an effective mechanism for scavenging waste heat [1,2] by developing efficient devices. Even after persistent efforts and investments, designing efficient thermoelectrics is reaching a plateau. The obtained efficiency is not up to the mark and hence is far from commercialization. The efficiency of TE material is characterized by a dimensionless parameter, namely *figure of merit* (FOM), denoted by ZT , which explicitly depends on the Seebeck coefficient, electrical conductance, temperature, and total thermal conductance [3]. For bulk systems, electrical and thermal conductances are correlated by the Wiedemann-Franz (W-F) law [4], which essentially restricts to have an efficient energy conversion. However, it is possible to achieve better TE performance in the nanoscale regime than the bulk ones, overshadowing the W-F law [3,5,6]. Extensive efforts have been made to study the thermoelectric phenomena exploring the charge degrees of freedom in the nanoscale regime with systems like quantum dots [7–11], nanowires [12–15], topological insulators [16,17], and also organic molecular junctions [18–21] including DNAs, proteins [22–26], etc.

On the other hand, compared to charge-based devices, spintronic devices are usually faster, more efficient, and have smaller dimensions where the electron's spin allows us to perform more work providing much less effort [27–31]. A recent

development in the field of thermoelectric has been the entry of spin degrees of freedom, and magnetic order provides a “green” strategy to enhance the thermoelectric figure of merit [32]. This is due to the fact that the TE efficiency is directly proportional to the square of the Seebeck coefficient [33], and for a spin TE, it is defined as the difference between the contributions from the up and down spins. Interestingly, for the spin TE case, it is possible to achieve different signs of the spin-Seebeck coefficient, which can add up to produce a favorable TE response. Precisely, the spin-Seebeck effect (SSE) [34,35] is the charge analog of the Seebeck effect, where one can generate a net spin current from the temperature gradient and can potentially reduce the thermal dissipation induced by the total charge current [36–38]. One of the remarkable features of the spin-Seebeck device is that it possesses a scalability different from that of usual charge-based Seebeck devices, where the output power is proportional to the length perpendicular to the temperature gradient. Not only that, the heat current and charge current follow separate paths in the spin-based Seebeck device compared to the charge-based Seebeck device, which prompts us to think about that the spin Seebeck device as a possible route to enhance the thermoelectric FOM [39]. These salient features have invigorated spintronic research to develop spin-based TE devices [40–42].

The primary requirement of a spintronic device is to look for an efficient mechanism that sets apart the charge carriers based on their spin quantum number, which essentially means achieving polarized spin current from a completely unpolarized electron beam. Among several propositions [43–45], the most studied one is the use of ferromagnetic material as a functional element [46]. However, there are several limitations to overcome in that case, like a large resistivity mismatch is induced across the junction formed by ferromagnetic and nonmagnetic materials, which acts against the flow of the injected electrons [46,47]. Another major issue is the tuning of

*kallolsankarmondal@gmail.com

†sudinganguly@gmail.com

‡santanu.maiti@isical.ac.in

spin-selective junction currents under the application of external magnetic fields. Experimentally, it is hard to achieve such strong confinement of magnetic fields within the quantum regime. Due to the above-mentioned limitations, in the recent past, the focus is shifted towards spin-orbit (SO) coupled systems instead of ferromagnetic materials. The investigation along the line is dominated by Rashba SO coupled system over the Dresselhaus one, as the strength of the former one can be tuned externally by suitable setups [48,49]. Extensive efforts have been made in this regard to explore a range of different geometries using inorganic and organic molecules [50–52]. But it turns out that, especially in molecular systems, the strength of the SO coupling is significantly weak compared to the hopping strength, differing by order of magnitude [53]. In addition to that, the tuning of SO coupling strength is also restricted by external means. As a result, it is difficult to obtain a high degree of spin separation and its possible tuning in a wide range in those spin-orbit coupled systems.

Due to the aforementioned issues with ferromagnetic systems, there is a growing inclination towards antiferromagnetic materials for future spintronic applications [54–56]. Antiferromagnets are magnetically ordered, with the nearest-neighbor spins aligning in the opposite direction resulting in net zero magnetic moments. Thus these types of magnetic structures are robust against external perturbations like magnetic fields, produce no stray fields, display ultrafast dynamics, and are capable of generating large magnetotransport effects [57]. Intensive efforts have been made to unravel the spin transport properties in antiferromagnetic materials, and antiferromagnetic spintronics remains an active area of cutting-edge research [58–61].

Recent experiments have made significant progress along this line, considering different kinds of helical molecules [62]. It has been established that the helicity plays the central role for efficient spin filtration and the phenomenon is commonly referred to as chiral-induced spin selectivity (CISS) effect. This unconventional CISS effect [63–68] led us to think about exploring chiral molecules in different spintronic applications.

In the present communication, we propose a new prescription for efficient thermoelectric response, considering an antiferromagnetic helix as a functional element in the presence of the transverse electric field. To the best of our knowledge, no effort has been made to understand thermoelectric physics in such systems. We extensively study the charge and spin-dependent thermoelectric responses on a single-stranded antiferromagnetic helix system connected by two one-dimensional (1D) nonmagnetic, reflectionless, semi-infinite leads in the presence of a transverse electric field (see Fig. 1). We simulate the whole system using the tight-binding framework. We employ nonequilibrium Green's function (NEGF) formalism following the Landauer-Buttiker prescription to study the thermoelectric phenomena [69–72]. It is a well-known fact that no spin separation is possible for antiferromagnetic systems with zero net magnetization, but it is possible to generate spin filtration under the application of a transverse electric field. The physics of spin filtration solely depends on the interplay between the helicity of the antiferromagnetic helix (AFH) and the applied electric field. For a precise estimation of the TE response, we include the

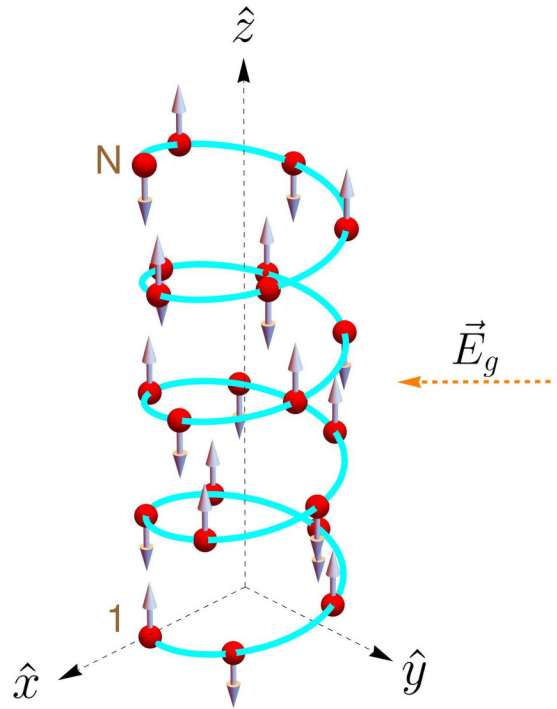


FIG. 1. Schematic diagram of an antiferromagnetic right-handed helix. Each red ball corresponds to a magnetic site and the arrow on the ball represents the direction of magnetic moment. Perpendicular to the helix axis, an external electric field is applied, which plays a central role in our investigation.

phonon contribution in the present case. In the pursuit of a more profound theoretical comprehension of the influence of various factors, including the strength and orientation of the electric field, as well as several geometric parameters inherent to helical systems, etc., we conduct a meticulous and critical examination of their impact on the thermoelectric behavior. To prove the robustness of our analysis, we compute the results by varying the physical parameters in a wide range. All the results are critically explained with proper physical arguments. For the sake of completeness of our study, we also provide experimental possibilities of our chosen antiferromagnetic helix. Our prescription shows a favorable spin-dependent thermoelectric response as compared to the charge counterpart at room temperature.

The rest part of the present communication is organized as follows. In Sec. II, we discuss the system along with the relevant interactions considered in the model and present the theoretical framework. In Sec. III, we have meticulously scrutinized all the results obtained while considering both short-range and long-range hoppings in the presence of an electric field. Finally, in Sec. IV, we conclude our essential findings.

II. THEORETICAL FORMULATION

A. Description of the system

Let us first introduce the system to study the thermoelectric phenomena. Figure 1 depicts the schematic diagram of

TABLE I. Geometrical parameters for the helical systems.

System type	Radius (R)	Stacking distance (Δz)	Twisting angle ($\Delta\phi$)	Decay constant (l_c)
SRH	7 Å	3.4 Å	$\pi/5$ rad	0.9 Å
LRH	2.5 Å	1.5 Å	$5\pi/9$ rad	0.9 Å

our proposed single-stranded antiferromagnetic helix which contains N magnetic sites. The helix is coupled to two 1D non-magnetic, reflectionless, semi-infinite leads, namely source (S) and drain (D) (not shown in Fig 1) at site 1 and site N respectively. These two leads are operating at two different temperatures, $T + \Delta T$ and $T - \Delta T$, where T is the equilibrium temperature and ΔT is infinitesimally small. Thus we restrict ourselves within the linear response regime throughout the analysis.

We use helical system as a functional element to study the TE response. In general, a helical system is described by two important parameters like stacking distance and twisting angle, denoted by Δz and $\Delta\phi$, respectively [63,64]. These two parameters play a crucial role in determining whether the hopping is short-range or long-range and also determine the structure of the magnetic helix. When Δz is very small, the atomic sites are closely spaced, and the electrons can hop to higher-order neighbor sites, yielding a long-range hopping (LRH) helix. On the other hand, when Δz is quite large, the hopping of the electrons is restricted mostly to a few neighboring sites, and we have short-range hopping (SRH) helix. Here, we present the parameter values for a typical case of SRH and LRH systems in Table I (for the details of the helical geometry and relevant parameters, one may look at the pioneering work [64]).

These geometrical parameters are inspired by DNA and α -proteins, respectively, and are the most suitable examples where the short-range hopping and long-range hopping can be explored. Here it is relevant to mention that these parameters are not directly involved with DNA and α -protein molecules.

In our chosen antiferromagnetic helix system, the successive magnetic moments are aligned along $\pm z$ directions, and thus the resultant magnetization becomes zero. Each magnetic site i is associated with a net spin $\langle \mathbf{S}_i \rangle$. The general orientation of any such spin vector can be described by the usual polar angle θ_i and the azimuthal angle φ_i . Now, the incoming electron will interact with these local magnetic moments through the usual spin-moment exchange interaction J . To include this interaction, we introduce a spin-dependent scattering (SDS) parameter at each site i as $\hat{h}_i = J \langle \mathbf{S}_i \rangle$ [53]. The strength of the SDS parameter $|\hat{h}_i|$ is assumed to be isotropic, i.e., $\hat{h}_i = \hat{h} \forall i$. For the present investigation, the interaction between neighboring magnetic moments is ignored, and it is a subject of future study.

The central region, i.e., the AFH, is exposed to an electric field, having strength E_g , perpendicular to the helix axis (\hat{z}) as shown in Fig. 1. The incorporation of electric field in our theoretical formalism is described in the forthcoming section.

B. Model Hamiltonian

The tight-binding Hamiltonian representing the total system comprises four parts, which are given by [73–76]

$$\mathcal{H} = \mathcal{H}_{\text{AFH}} + \mathcal{H}_S + \mathcal{H}_D + \mathcal{H}_C, \quad (1)$$

where, \mathcal{H}_{AFH} , \mathcal{H}_S , \mathcal{H}_D , and \mathcal{H}_C represent the subparts of the Hamiltonian, associated with the AFH, source, drain, and the coupling between the leads and the AFH, respectively.

The Hamiltonian for the AFH is given by [68,77]

$$\begin{aligned} \mathcal{H}_{\text{AFH}} = & \sum_n \mathbf{c}_n^\dagger (\epsilon_n - \hat{h}_n \cdot \boldsymbol{\sigma}) \mathbf{c}_n \\ & + \sum_n \sum_m^{N-1, N-n} (\mathbf{c}_n^\dagger \mathbf{t}_n \mathbf{c}_{n+m} + \text{H.c.}), \end{aligned} \quad (2)$$

where \mathbf{c}_n denotes the two-component fermionic operator at site n , given by $\mathbf{c}_n = \begin{pmatrix} c_{n\uparrow} \\ c_{n\downarrow} \end{pmatrix}$ and its hermitian counterpart \mathbf{c}_n^\dagger is defined accordingly. $\boldsymbol{\sigma}$ is the well-known Pauli matrices, \mathbf{t}_n and ϵ_n are the 2×2 diagonal matrices given by

$$\mathbf{t}_n = \begin{pmatrix} t_n & 0 \\ 0 & t_n \end{pmatrix} \quad \text{and} \quad \epsilon_n = \begin{pmatrix} \epsilon_n & 0 \\ 0 & \epsilon_n \end{pmatrix}, \quad (3)$$

where ϵ_n is the on-site energy in the absence of any spin-dependent scattering and t_n represents the hopping amplitude from the site n to $n + m$. The inclusion of SDS leads to the effective site energy matrix $(\epsilon_n - \hat{h}_n \cdot \boldsymbol{\sigma})$. Now, the presence of an external electric field E_g , perpendicular to the helix axis, modifies the on-site energy in the following way [68,77]:

$$\epsilon_n^{\text{eff}} = \epsilon_n + eV_g \cos(n\Delta\phi - \beta), \quad (4)$$

where e is the electronic charge, $V_g (= 2E_g R)$ is the applied gate voltage, and β is the angle between the incident electric field and the positive \hat{x} axis, R is the radius of the helix.

Due to the helical shape of the physical system, the hopping term becomes quite tricky, unlike the usual nearest-neighbor hopping (NNH) case. The summations over the site indices are to be taken carefully. The expression for the hopping integral t_n is given by

$$t_n = t_1 \exp[-(l_n - l_1)/l_c], \quad (5)$$

where t_1 and l_1 are the nearest-neighbor hopping amplitude and the distance among the nearest-neighbor sites, respectively. l_c is the decay constant and l_n is the spatial separation between the sites n and $n + m$. The expression of l_n is given by

$$l_n = [(2R \sin(n\Delta\phi/2))^2 + (n\Delta z)^2]^{1/2}, \quad (6)$$

where Δz and $\Delta\phi$ are the stacking distance and twisting angle, respectively.

The contributions from the leads and the coupling between the leads and the central region to the total Hamiltonian read as

$$\mathcal{H}_S = \sum_{m<1} \mathbf{a}_m^\dagger \epsilon_0 \mathbf{a}_m + \sum_{m<1} (\mathbf{a}_m^\dagger \mathbf{t}_0 \mathbf{a}_{m-1} + \text{H.c.}), \quad (7a)$$

$$\mathcal{H}_D = \sum_{m>N} \mathbf{b}_m^\dagger \epsilon_0 \mathbf{b}_m + \sum_{m>N} (\mathbf{b}_m^\dagger \mathbf{t}_0 \mathbf{b}_{m+1} + \text{H.c.}), \quad (7b)$$

$$\mathcal{H}_C = \mathbf{a}_0^\dagger \boldsymbol{\tau}_S \mathbf{c}_1 + \mathbf{c}_N^\dagger \boldsymbol{\tau}_D \mathbf{b}_{N+1} + \text{H.c.} \quad (7c)$$

Here, $\mathbf{a}_n, \mathbf{b}_n$ are used for the source and the drain in the same way like the \mathbf{c}_n operator. ϵ_0 and \mathbf{t}_0 are 2×2 diagonal matrices where the on-site potential ϵ_0 and hopping amplitude t_0 are taken to be the same for both the leads. The coupling between the source (drain) and the AFH is denoted by τ_S (τ_D), defined in the same footing as \mathbf{t}_0 .

C. Two-terminal transmission probability

We employ NEGF formalism to evaluate the two-terminal transmission probability through the helix system. The standard way to put up the retarded Green's function for the present case is as follows:

$$\mathcal{G}^r = [(E + i0^+)\mathbb{I} - \mathcal{H}_{\text{AFH}} - \Sigma_{\sigma S} - \Sigma_{\sigma D}]^{-1}, \quad (8)$$

where σ, σ' are the spin indices, $\Sigma_{\sigma S}$ and $\Sigma_{\sigma D}$ represent the contact self-energies of the source and drain, respectively, \mathbb{I} is the identity matrix with dimension $2N \times 2N$. The rest of the other symbols have the usual meaning.

Now, the transmission probability can be expressed in terms of retarded (\mathcal{G}^r) and advanced ($\mathcal{G}^a (= \mathcal{G}^r)^\dagger$) Green's functions as

$$\mathcal{T}_{\sigma\sigma'} = \text{Tr}[\Gamma_{\sigma S} \mathcal{G}^r \Gamma_{\sigma' D} \mathcal{G}^a], \quad (9)$$

where $\Gamma_{\sigma S}$ and $\Gamma_{\sigma D}$ are the coupling matrices that describe the rate at which particles scatter between the leads and the AFH. $\mathcal{T}_{\sigma\sigma'}$ indicates the probability of a transmitted electron with spin σ' injected with spin σ . We must mention that if $\sigma = \sigma'$, then we get pure spin transmission, otherwise we get a spin-flip transmission. We define the net up and down spin transmission probabilities as

$$\mathcal{T}_\sigma = \sum_{\sigma'} \mathcal{T}_{\sigma'\sigma}, \quad (10)$$

where σ and σ' can be either \uparrow or \downarrow . These are fundamental entities to calculate different thermoelectric quantities as described in the next section.

D. Thermoelectric quantities

In the linear response regime, all the spin-resolved thermoelectric quantities like the electrical conductance G_σ , Seebeck coefficient (thermower) S_σ , and electrical conductance $k_{\sigma\text{el}}$ can be extracted using Landauer's integrals as [78,79]

$$G_\sigma = \frac{e^2}{h} L_{0\sigma}, \quad (11a)$$

$$S_\sigma = -\frac{1}{eT} \frac{L_{1\sigma}}{L_{0\sigma}}, \quad (11b)$$

$$k_{\sigma\text{el}} = \frac{1}{hT} \left(L_{2\sigma} - \frac{L_{1\sigma}^2}{L_{0\sigma}} \right), \quad (11c)$$

where spin-resolved Landauer's integral $L_{n\sigma}$ ($n = 0, 1, 2$) is given by

$$L_{n\sigma} = - \int \mathcal{T}_\sigma(E) (E - E_F)^n \frac{\partial f_{\text{FD}}}{\partial E} dE, \quad (12)$$

where, h , f_{FD} , and E_F denote Planck's constant, equilibrium Fermi-Dirac occupation probability, and Fermi energy, respectively. Here, $\mathcal{T}_\sigma(E)$ is the spin-resolved two-terminal transmission probability as defined earlier.

Now, we define the charge (c) and spin (s) electrical conductances in the following way [80]:

$$G_c = G_\uparrow + G_\downarrow \quad \text{and} \quad G_s = G_\uparrow - G_\downarrow. \quad (13)$$

The charge and spin Seebeck coefficients (thermopowers) are defined by [80,81]

$$S_c = \frac{1}{2}(S_\uparrow + S_\downarrow) \quad \text{and} \quad S_s = (S_\uparrow - S_\downarrow). \quad (14)$$

Similarly, the charge and spin thermal conductances are given by [80]

$$k_{\text{cel}} = k_{\text{sel}} = (k_\uparrow + k_\downarrow). \quad (15)$$

The charge and spin *figure of merits* can be expressed in a compressed form in the following way [80]:

$$Z_\alpha T = \frac{|G_\alpha| S_\alpha^2 T}{k_\alpha}, \quad (16)$$

where α ($= c, s$) stands for the charge and spin degrees of freedom. $k_\alpha = k_{\alpha\text{el}} + k_{\text{ph}}$, where k_{ph} is the phonon contribution to the total thermal conductance. Typically, a thermoelectric response of the order of unity is often regarded as favorable TE response. However, for an economically competitive response, $Z_\alpha T \sim 3$ is often prescribed [82]. For a precise estimation of $Z_\alpha T$, one needs to consider the contribution of k_{ph} in thermal conductance. The method for calculating k_{ph} is given in the forthcoming section.

E. Calculation of phonon thermal conductance

When the temperature difference between the two contact leads is infinitesimally small, the phonon thermal conductance in the NEGF formalism can be evaluated from the expression [83–86]

$$k_{\text{ph}} = \frac{\hbar}{2\pi} \int_0^{\omega_c} \mathcal{T}_{\text{ph}} \frac{\partial f_{BE}}{\partial T} \omega d\omega. \quad (17)$$

Here, ω is the phonon frequency and ω_c the phonon cutoff frequency, respectively. We consider only elastic scattering in the present case. f_{BE} denotes the Bose-Einstein distribution function. \mathcal{T}_{ph} is the phonon transmission probability across the central region, evaluated through the NEGF formalism as

$$\mathcal{T}_{\text{ph}} = \text{Tr}[\Gamma_S^{\text{ph}} \mathcal{G}_{\text{ph}} \Gamma_D^{\text{ph}} (\mathcal{G}_{\text{ph}})^\dagger]. \quad (18)$$

$\Gamma_{S/D}^{\text{ph}} = i[\tilde{\Sigma}_{S/D} - \tilde{\Sigma}_{S/D}^\dagger]$ is known as the thermal broadening. $\tilde{\Sigma}_{S/D}$ is the self-energy matrix for the source/drain lead. The phononic Green's function for the AFH reads as

$$\mathcal{G}_{\text{ph}} = [\mathbb{M}\omega^2 - \mathbb{K} - \tilde{\Sigma}_S - \tilde{\Sigma}_D]. \quad (19)$$

Where \mathbb{M} is a diagonal matrix that describes the mass matrix of the helix. Each element of the mass matrix \mathbb{M}_{mm} denotes the mass of the n th atom in the helical system and \mathbb{K} is the matrix of spring constants. The diagonal element \mathbb{K}_{nn} denotes the restoring force of the n th atom due to its neighboring atoms, while the element \mathbb{K}_{nm} represents the effective spring constant between n th and m th neighboring atoms. The self-energy matrices $\tilde{\Sigma}_S$ and $\tilde{\Sigma}_D$ have the same dimension as \mathbb{M} and \mathbb{K} and can be computed by evaluating the self-energy term $\Sigma_{S/D} = -K_{S/D} \exp[2i \sin^{-1}(\frac{\omega}{\omega_c})]$, where $K_{S/D}$ is the spring constant at the lead-helix contact interface.

The spring constants are determined from the second derivative of Harrison's interatomic potential [87]. Since a 1D system does not allow any transverse interaction [88], the spring constant for the 1D lead is given by $K = 3dc_{11}/16$. For a 3D system like helix, the spring constant is $K = 3d(c_{11} + 2c_{12})/16$. Here d denotes the interatomic spacing and c_{11} and c_{12} are the elastic constants. The cutoff frequency for the 1D lead is determined from the relation $\omega_c = 2\sqrt{K/M}$, in terms of the mass and spring constant.

III. NUMERICAL RESULTS AND DISCUSSION

The interplay between the transverse electric field and the helicity plays the central role to have spin-dependent TE phenomena in our chosen antiferromagnetic helix which we are going to discuss in this section. In the absence of any of these two parameters viz. the helicity and the electric field, there will be no mismatch between up and down spin channels, and therefore, we cannot expect any spin-dependent transport phenomena. The underlying physical mechanism is as follows. As all the magnetic moments are aligned along $\pm\hat{z}$ directions, the Hamiltonian of the antiferromagnetic helix can be decoupled as a sum of up and down spin Hamiltonians (viz. $H_\uparrow + H_\downarrow$). In the absence of electric field, these two sub-Hamiltonians are symmetric to each other, because of the antiparallel configuration of the successive magnetic moments, resulting identical set of energy eigenvalues. The symmetry can be broken quite easily by applying an electric field in the helix system. Under that condition, we have a finite mismatch between the two different spin-dependent energy channels.

In presence of transverse electric field, the site energies get modulated in a cosine form as mentioned in Eq. (4). The site energy expression looks identical to the well-known Aubrey-André-Harper (AAH) model [89]. In the AAH model, the on-site term reads as $\epsilon_n = W \cos(2\pi bn + \phi_v)$ (n being the site index), where W is the AAH modulation strength, b is an irrational number, and ϕ_v is the AAH phase. The one-to-one mapping is obvious in view of Eq. (4), where one identifies the term eV_g as the AAH modulation strength W , $2\pi b$ as the twisting angle $\Delta\phi$, and β as the AAH phase factor ϕ_v . Thus one can capture the essential physics of the AAH model using the above formulation through our helical system.

Before discussing the results, let us first mention that the present communication focuses on the right-handed helices. All the energies are measured in the units of eV. In the absence of any electric field, the on-site energies ϵ_n in the AFH are fixed to zero, and we choose the NNH strength $t_1 = 1$ eV. For the leads, we choose $\epsilon_0 = 1$ eV and $t_0 = 2.5$ eV. To work in the wide-band limit [90], we set $t_0 > t_1$. The reason behind the consideration of wide-band limit is that no allowed energy channel of the helix which is clamped between the contact leads is missed. So the basic requirement is that the allowed energy window ($\epsilon_0 - 2t_0 \leq E \leq \epsilon_0 + 2t_0$) of the leads must be always higher than the available energy region of the helix system. Here we would like to point out that the choice of $\epsilon_0 = 1$ eV is not unique, any other value of ϵ_0 can be taken into account satisfying the above mentioned condition. The coupling strengths between the central region to the source and drain leads, characterized by the parameters τ_S and τ_D , are fixed at 0.8 eV. For any other choices of the tight-binding parameter

values (except the coupling constants), the physical pictures qualitatively remain the same, which we confirm through our exhaustive numerical calculation. Now we present our results one by one as follows.

A. Energy eigenvalues and transmission spectra

Let us begin our discussion by examining the spectral behavior of the AFH in the presence of an electric field. In Fig. 2(a), we present the eigenspectra of a typical short-range hopping AFH considering $N = 20$, where we set $\hbar = 0.5$, $V_g = 1$, and $\beta = 0$. The energy spectra for the up and down spins are depicted in red and black, respectively. Notably, the spectra for the up and down spins are nondegenerate. Similarly, in Fig. 2(b), we display the eigenspectrum of a long-range AFH while keeping the parameters the same as in the short-range case. Once again, we observe that the spectrum for the two opposite spin states are nondegenerate. Furthermore, in each of these spectra, a noticeable energy gap is observed at multiple regions, and this is the generic feature of a correlated disordered system. What is particularly noteworthy is that in both scenarios, a nonzero spin separation is observed in the presence of an electric field and a spin-dependent scattering parameter. It is essential to emphasize that when the electric field strength is set to zero, such a separation among the energy eigenvalues for up and down spins does not occur. This is owing to the fact that the up and down spin sub-Hamiltonians are symmetric to each other for the field-free case.

The observed channel separation implies that there exists a finite disparity between the transmission probabilities for up and down spins, which is a crucial prerequisite for the emergence of spin FOM. To illustrate this phenomenon, in Fig. 3, we depict the spin-resolved transmission probabilities as a function of energy. The transmission probabilities for up and down spin channels are represented by the red and black curves, respectively, as shown in Fig. 3(a) for the SRH and Fig. 3(b) for the LRH. The system size and other parameters are kept identical to those in Fig. 2. The transmission spectra for both up and down spins in the SRH and LRH helices are distinct from each other. These transmission spectra exhibit a gapped nature [77,91] due to the presence of the electric field, which acts as a correlated disorder within the system, as discussed earlier.

To achieve a favorable spin TE response, the spin-resolved transmission spectrum must satisfy two critical conditions. Firstly, the transmission spectrum should display asymmetry around a fixed energy [92,93]. This first criterion is a general requirement applicable to both charge and spin TE responses. Secondly, it is desirable to have crossings between the up and down spin transmission spectra. In Figs. 3(a) and 3(b), we have highlighted some of these crossings with blue-dotted ellipses and provided insets for clarity. For instance, in Fig. 3(a), around the energy of 1.4 eV, a sharp peak is observed in the down-spin transmission on the left side of the crossing, while the up-spin transmission spectrum exhibits a sharp peak on the right side. This sharp peak creates an asymmetry in the transmission function, and the presence of such crossings guarantees a substantial spin thermopower. We will delve into this aspect in greater detail in the context of thermopower in the next section.

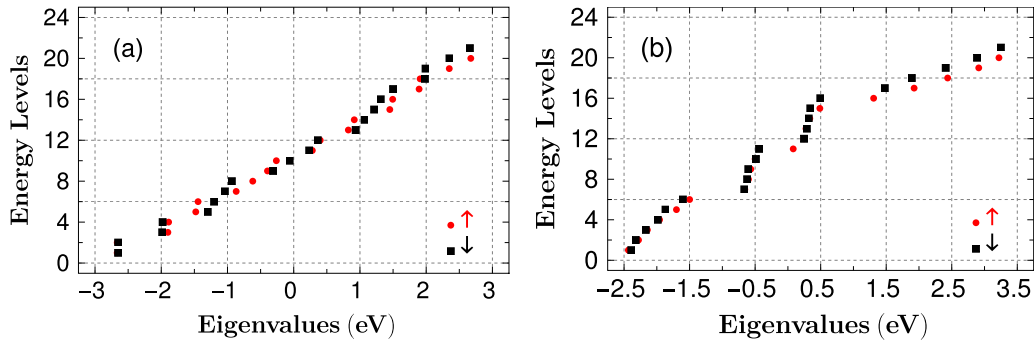


FIG. 2. Eigenvalue spectrum in presence of the electric field in case of (a) short-range hopping and (b) long-range hopping with $\hbar = 0.5$, $V_g = 1$, and $\beta = 0$. The horizontal axis represents the eigenvalues of the AFH and the vertical axis denotes the energy labels. The energy labels of the eigenvalues corresponds to sorting them in ascending order and then assigning sequential numbers. The number of sites in the helix is $N = 20$. The eigenvalues for the up and down spins are represented by red and black colors, respectively.

B. Thermoelectric quantities

Now, let us proceed to analyze various TE quantities, such as electrical conductance, thermopower, thermal conductance, and the FOM, at room temperature ($T = 300$ K). We explore both the charge and spin TE properties for the SRH and LRH helices. The TE phenomena are critically discussed under different input conditions, by varying the physical parameters associated to the systems in a wide range, to check the robustness of our analysis.

The variation of electrical conductance G_α (in units of e^2/h) with Fermi energy E_F is illustrated in Figs. 4(a) and 4(d) for the SRH and LRH helices, respectively, where α represents charge and spin. In Fig. 4(a), we observe that both charge and spin-dependent electrical conductances (represented by the red and green curves, respectively) exhibit nearly symmetric behavior around the $G_\alpha = 0$ line for the short-range helix. The maximum value of $|G_\alpha|$ is approximately 0.46, and it diminishes significantly beyond $E_F \sim 1.4$ eV. This behavior can be elucidated by referring to the transmission profile of the SRH case [Fig. 3(a)].

It is important to note that the total charge electrical conductance is defined as the sum of contributions from the up and down spin channels, whereas the spin counterpart is calculated as the difference between the two. The opposite signs of charge and spin G_α below $E_F \sim 1.4$ eV imply that the contribution from the up-spin channel is exceedingly small in

this Fermi energy range. This phenomenon arises from the fact that the up-spin transmission probability is negligibly small compared to the down-spin transmission probability, as evident from Fig. 3(a). Moving into the Fermi energy range from ~ 1.4 to ~ 2 , we observe that both up and down transmission probabilities become small, resulting in nearly negligible G_α values, as depicted in Fig. 4(a).

The LRH helix, under the same set of parameters, exhibits somewhat analogous behavior, as observed in Fig. 4(d), mirroring the characteristics of the up and down spin transmission spectra depicted earlier.

As TE efficiency is directly proportional to the square of thermopower, a large thermopower (S) is always desirable. In the case of spin TE, it is possible to achieve two different signs of thermopower associated with up and down spin electrons, which can algebraically sum up to produce a larger value of the figure of merit. Therefore a proper selection of the Fermi energy becomes a critical consideration. To attain different signs of thermopower, one should seek a narrow Fermi energy window where the transmission function exhibits asymmetry. Moreover, the up and down spin channels must have slopes of opposite signs around this selected Fermi energy.

Thermopower is calculated using Eq. (11b) and the corresponding Landauer's integral L_1 , where the transmission function is multiplied by $(E - E_F)$ and $\frac{\partial f_{FD}}{\partial E}$. The latter term introduces thermal broadening, and the product of the

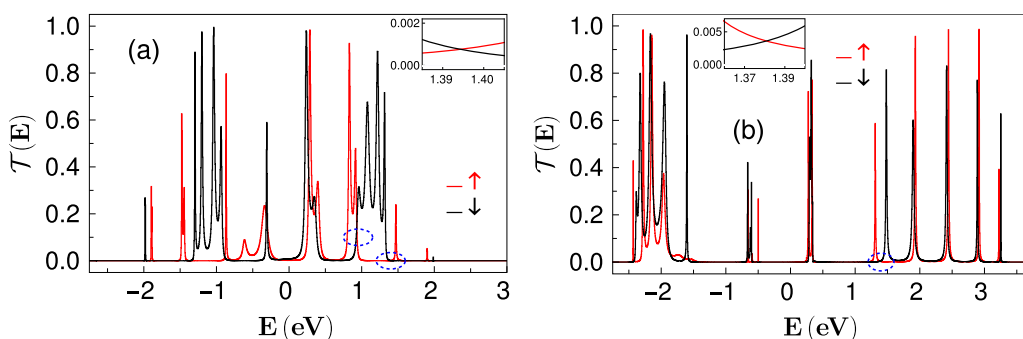


FIG. 3. Spin-resolved transmission probability as a function of energy for (a) short-range hopping and (b) long-range hopping. All the parameters and color conventions are the same as described in Fig. 2. The blue dotted ellipses mark the cross-over regions between up and down spin transmissions. In the insets, the crossover is more visible and also shows that the transmission probabilities are small but finite.

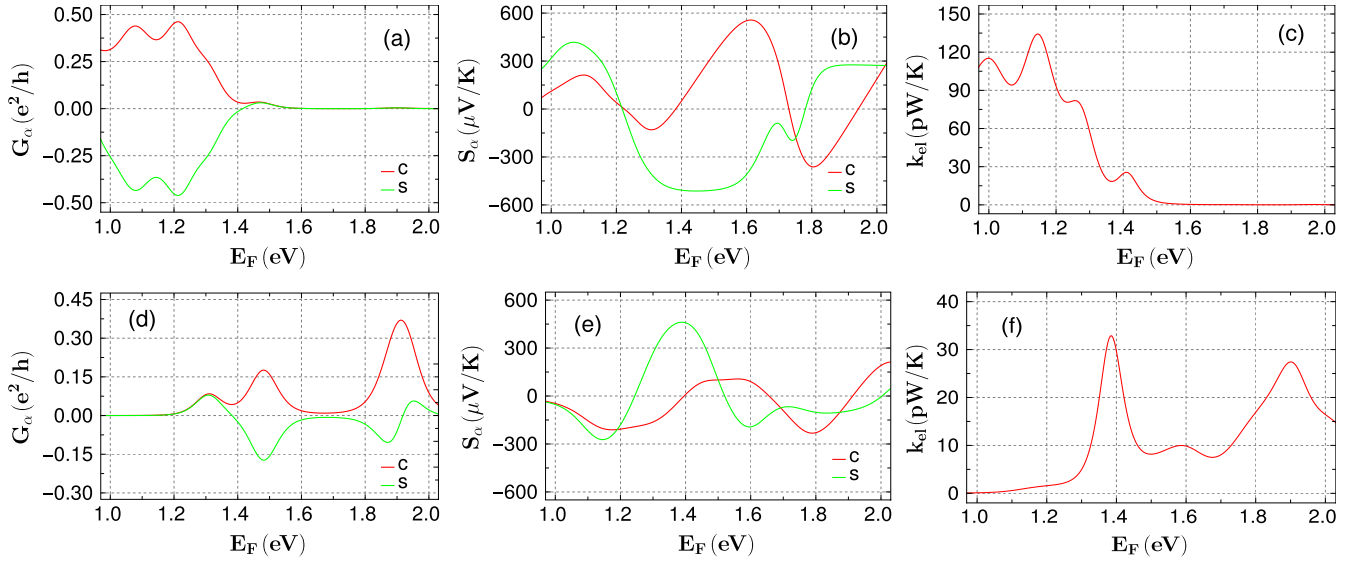


FIG. 4. Behavior of different thermoelectric quantities at room temperature $T = 300$ K as a function of Fermi energy. The upper panel shows the results for the SRH helix and the lower panel for the LRH one. In (a) and (d), electrical conductance (G_α), [(b) and (e)] thermopower (S_α), and [(c) and (e)] thermal conductance due to electrons (k_{ei}) are shown. All the parameters are the same as described in Fig. 2. The subscript α represents the charge (c) and spin (s) degrees of freedom and their corresponding results are shown by red and green curves, respectively.

two is antisymmetric about the chosen E_F . Consequently, if the transmission function is symmetric around E_F , the thermopower will be zero, regardless of the values of the transmission probabilities. However, if the slopes of the spin-resolved transmission functions have opposite signs around the chosen Fermi energy, the thermopower acquires a distinct sign and large values due to the asymmetric nature of $\mathcal{T}(E)$. This results in a significantly larger spin thermopower.

In Figs. 4(b) and 4(e), we depict the variation of thermopower with Fermi energy within the same energy window discussed earlier for electrical conductance in the cases of SRH and LRH, respectively. For the SRH helix, it is evident from the transmission profile [see Fig. 3(a)] that around $E \sim 1.4$, the up and down spin channels exhibit slopes of opposite signs, marked by the blue dotted ellipse in Fig. 3. This results in a large value of spin thermopower, as observed in Fig. 4(b). In contrast, the charge thermopower becomes very small at this Fermi energy since it is the algebraic sum of the up and down spins.

Similarly, the large value of spin thermopower in the LRH case, shown in Fig. 4(e), can be explained by the transmission profile. Here as well, the up and down spin channels display slopes of opposite signs at $E_F \sim 1.38$ eV, leading to a substantial spin thermopower compared to its charge counterpart. The maximum thermopower reaches approximately $600 \mu\text{V}/\text{K}$ for the SRH helix and $550 \mu\text{V}/\text{K}$ for the LRH helix.

The behavior of thermal conductance due to electrons as a function of Fermi energy is illustrated in Figs. 4(c) and 4(f) for the SRH and LRH helices, respectively. Within the specified Fermi energy range, the maximum thermal conductance reaches approximately ~ 135 pW/K, as depicted in Fig. 4(c), and decreases significantly beyond $E_F \sim 1.5$ eV. In the case of the LRH helix, thermal conductance is observed to have

lower values compared to SRH, with the maximum value reaching approximately 33 pW/K at around $E_F \sim 1.38$ eV.

The system sizes under consideration in this study are relatively small, typically on the order of a few nanometers. Consequently, it is expected that the thermal conductance due to phonons should have lower values compared to its electronic counterpart. However, for a precise estimation of the FOM, it is crucial to include the contribution from thermal conductance due to phonons, which we will now discuss.

C. Phonon contribution to thermal conductivity

Before we discuss the behavior of k_{ph} , one needs to mention the spring constants of the leads and the central helix molecule. The 1D leads are considered Au leads, whose spring constant is 14.68 N/m [94]. For the helix molecule, we consider the spring constant about 5.1 N/m, which is considered as same as the single-crystal benzene [95]. Here we assume that two different atoms are adjacent to each other at the interface, one type of atom accounts for the Au lead and the other type for the helix molecule. By averaging the spring constants of the leads and helix molecule, and the masses, the cutoff frequency for Au lead comes out to be $\omega_c = 13.7$ Trad/s. Here it should be noted that the spring constant for the helix molecule is chosen for a light molecule. However, if one works with heavy molecules, the phonon vibrations will be less than our case and therefore, k_{ph} is expected to have lower values, and hence larger ZT .

In Fig. 5(a), the phonon transmission probability is plotted as a function of phonon frequency. We observe a few Fabry-Pérot-like peaks [85]. The behavior of phonon thermal conductance with temperature is shown in Fig. 5(b). Within

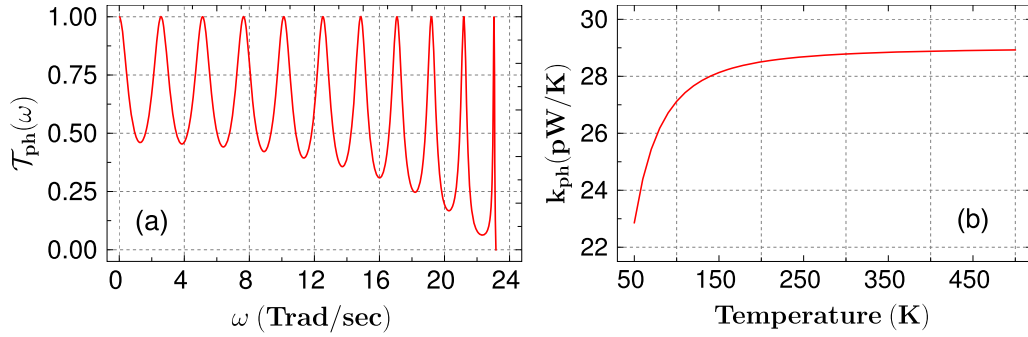


FIG. 5. (a) Phonon transmission probability \mathcal{T}_{ph} as a function of phonon angular frequency ω . (b) Phonon thermal conductance k_{ph} as a function of temperature T .

the temperature window 50 to 150 K, k_{ph} increases rapidly with temperature, and then it tends to saturate. The saturated value is about 29 pW/K.

D. Thermoelectric efficiency

After conducting a comprehensive analysis of various thermoelectric properties, including the consideration of phonon contributions, we calculate the charge and spin FOMs. These FOM values are plotted as a function of the Fermi energy for two distinct helix molecules, SRH and LRH, at room temperature. The results are depicted in Figs. 6(a) and 6(b) for the SRH and LRH helices, respectively.

Remarkably, our findings reveal that both SRH and LRH molecules exhibit highly favorable responses in spin FOM, significantly outperforming their charge counterparts. The maximum spin- ZT to be approximately 7 for SRH and around 4.5 for LRH cases. These peak values occur at Fermi energies of approximately 1.35 eV for SRH and 1.45 eV for LRH. These compelling results underscore the efficacy of our approach, demonstrating a remarkably favorable spin thermoelectric response.

So far, we have studied the TE results using specific parameter values for both the SRH and LRH molecules. Now, our focus shifts to investigating how various parameters, such as the spin-dependent scattering factor, electric field, helix characteristics, TB parameters, temperature, etc., influence the spin TE behavior. Notably, both the SRH and LRH

molecules have demonstrated promising spin TE responses. However, for the sake of the brevity of the presentation, we will concentrate solely on the LRH molecule in the following discussion. We have also observed analogous dependencies in the case of the SRH molecule, which we have duly confirmed through comprehensive numerical calculations. Consequently, we omit the results for the SRH molecule.

E. Role of spin-dependent scattering parameter

The dependence of the spin-dependent scattering parameter \hat{h} is examined in Fig. 7 for two distinct values, namely $\hat{h} = 0.25$ and 0.75 eV. We also include the previously considered value of \hat{h} ($\hat{h} = 0.5$ eV) for the purpose of comparison. The maximum spin FOM is observed to be around 2.3 for $\hat{h} = 0.25$ eV and 3 for $\hat{h} = 0.75$ eV, which is lower in comparison to the result corresponding to $\hat{h} = 0.5$ eV. It is important to note that the effective on-site potential at site n is the difference between the potential due to the applied electric field and the spin-dependent scattering parameter. We have set $V_g = 1$ V, which is the previously chosen value. In the case of $\hat{h} = 0.25$ eV, the spin-splitting effect is less pronounced, leading to a decrease in the spin FOM value. Conversely, when the spin-dependent factor is larger, that is, $\hat{h} = 0.75$ eV, the effective on-site potential is reduced. Consequently, this does not yield a favorable response. As we further increase \hat{h} , the net on-site potential begins to act as a stronger source of disorder in the system, eventually leading to the diminishing of the favorable response. This conclusion has been validated

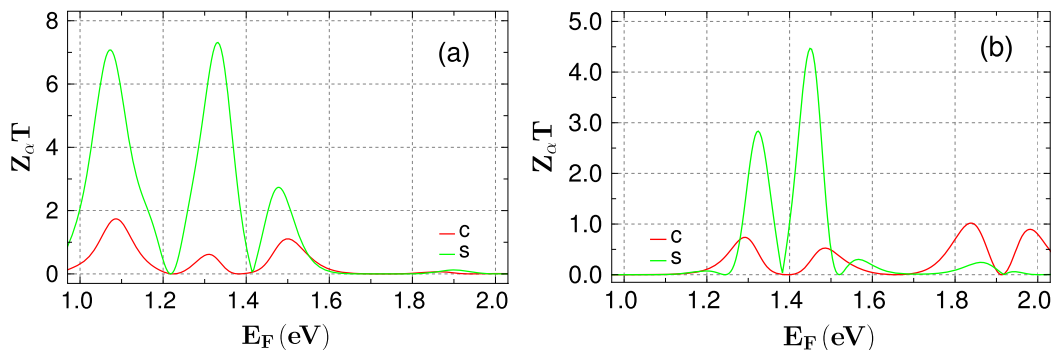


FIG. 6. Behavior of $Z_c T$ and $Z_s T$ as a function of Fermi energy at room temperature for (a) SRH and (b) LRH helices. All the parameters are considered as the same as in Fig. 2. The red and green curves represent the results for charge and spin FOMs, respectively.

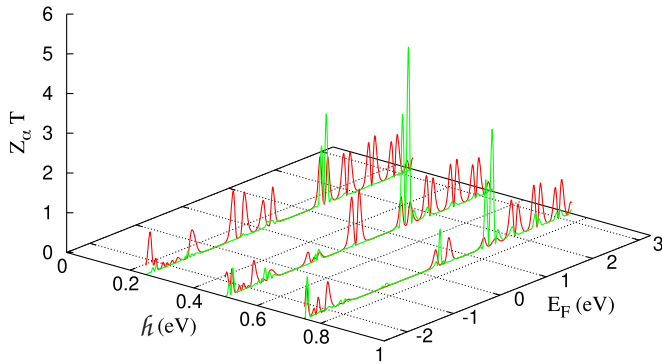


FIG. 7. Charge and spin thermoelectric FOMs as a function of Fermi energy for different \hat{h} values as shown by the red and green colors, respectively for LRH helix. The considered \hat{h} values are 0.25, 0.5 (included for comparison), and 0.75 eV. All the other parameters are identical with Fig. 2.

through our comprehensive analysis. In general, the spin TE response appears to be favorable for the selected values of \hat{h} .

F. Role of electric field

There are two factors concerning the electric field, namely, the intensity of the electric field, which corresponds to the applied gate voltage V_g , and the orientation of the field relative to the axis of the helical molecule β .

1. Effect of V_g

The behavior of charge and spin FOMs are illustrated with respect to the Fermi energy across two distinct gate voltages: $V_g = 0.5$ and 1.5 V, as depicted in Fig. 8.

For the sake of comparison, the plot includes the case of $V_g = 1$ V as well. The remaining parameters are identical with the description provided in Fig. 2 for the LRH molecule. Notably, for $V_g = 0.5$ and 1.5 V, the spin FOM displays favorable trends, with $Z_S T \sim 3$, confined within the Fermi energy range spanning from 1 to 2 eV.

It is important to note that, as previously mentioned, the gate voltage operates analogously to the strength of the AAH

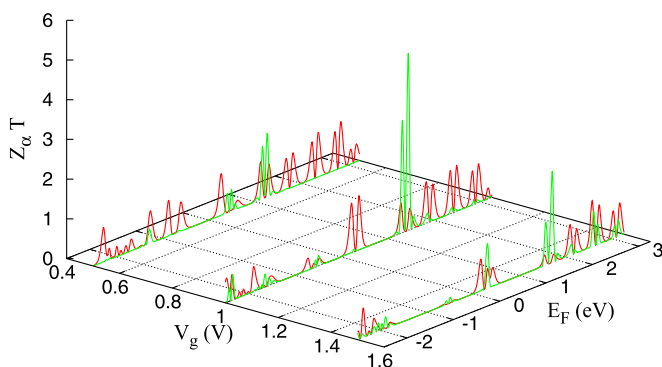


FIG. 8. Charge and spin FOMs as a function of Fermi energy for different values of V_g as shown by red and green colors, respectively for LRH helix. All the other parameters are identical to those in Fig. 2. Considered gate voltages are $V_g = 0.5$, 1 (included for comparison) and 1.5 V.

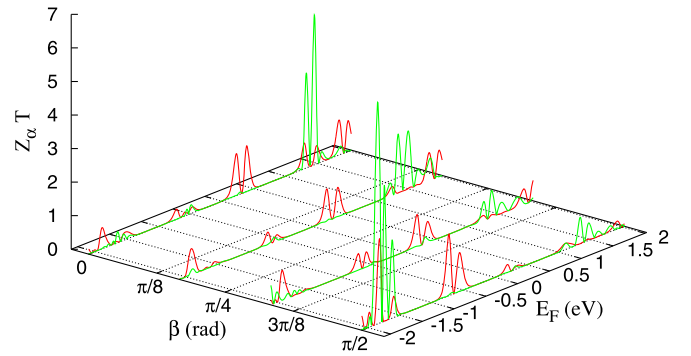


FIG. 9. Variation of charge and spin FOMs as a function of Fermi energy for different values of β as shown by red and green colors, respectively for LRH helix. All the parameters are identical to those in Fig. 2. β values are considered as $\beta = \pi/6$, $\pi/3$, and $\pi/2$. $\beta = 0$ is included for comparison.

disorder. Consequently, an anticipated outcome is that as the gate voltage increases, the system localization will intensify. Thus, beyond a certain threshold value of V_g , the observed favorable spin response will diminish. This is also true for the charge counterpart.

2. Effect of β

Till now, the direction of the electric field was assumed to be parallel to the positive \hat{x} axis, that is $\beta = 0$. To study the effect of β on TE performance, we consider other three different angles, namely, $\beta = \pi/6$, $\pi/3$, and $\pi/2$. The result for $\beta = 0$ is also included for comparison. Figure 9 shows the variation of charge and spin FOMs in the case of LRH at room temperature as a function of Fermi energy for different values of β . All other parameters are kept fixed, as stated earlier. The variation of $Z_{\alpha}T$ as a function of Fermi energy varied from -2.5 to 3.5 eV, which is the full energy window as shown in Fig. 2. Mostly, in all the cases, spin- ZT shows favorable response at different Fermi energies. Maximum spin- ZT is noted about 4.5, 1.75, 0.8, and 6.58 for $\beta = 0$, $\pi/6$, $\pi/3$, and $\pi/2$, respectively. Interestingly, maximum values of spin- ZT dominate over the charge- ZT for all the β values considered here.

G. Effect of helix parameters

The helical configuration is influenced by several key parameters: the radius R , twisting angle $\Delta\phi$, stacking distance Δz , and the decay constant l_c . We will now examine the impact of each of these parameters on the TE properties individually.

1. Role of R

Figure 10 illustrates the influence of the helix radius on both the charge and spin FOMs. We consider the cases of $R = 2$ and 3 Å, along with 2.5 Å for the purpose of comparison. It is important to note that altering the radius leads to variations in the distances between neighboring sites, consequently impacting the associated hopping integrals. Interestingly, across all the radius values considered here, the spin FOM consistently outperforms its charge counterpart

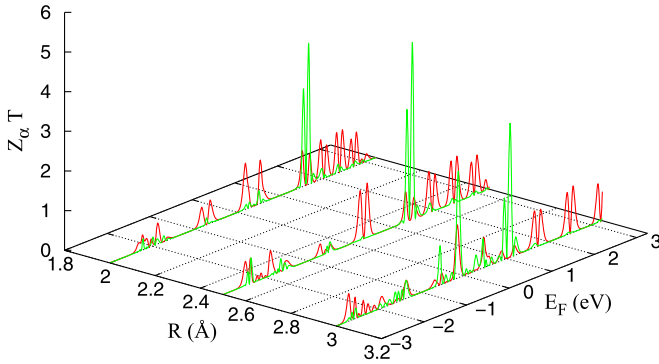


FIG. 10. Charge and spin thermoelectric FOMs as a function of Fermi energy for different radius of the LRH helix, as shown by the red and green colors, respectively. The considered radius values are $R = 2, 2.5$ (included for comparison), and 3 Å. All the other parameters are identical with Fig. 2.

within the Fermi energy window of 0 to 1 eV. The highest achieved spin FOM for radii of 2, 2.5, and 3 Å are notably impressive, reaching approximately 3.6, 4.5, and 3.4, respectively. It is worth noting that the charge ZT also remains above unity for all the different radius values considered. Overall, altering the radius of the helix continues to yield a highly favorable response in our study.

2. Role of $\Delta\phi$

The impact of the twisting angle $\Delta\phi$ on the TE behavior is investigated in Fig. 11. Our analysis considers two distinct twisting angles: $\Delta\phi - \delta$ and $\Delta\phi + \delta$, in addition to the previously examined case of

$\Delta\phi = 5\pi/9$. Here δ is fixed at a smaller value of 5° . It is important to note that even a slight alteration in the twisting angle can result in significant geometrical changes within the helix structure. Therefore we limit our investigation to slight modifications in $\Delta\phi$ to effectively observe its effects, while minimizing any substantial distortion to the geometric configuration. For both $\Delta\phi - \delta$ and $\Delta\phi + \delta$ cases (where $\delta = 5^\circ$), we consistently observe favorable responses. Notably, the

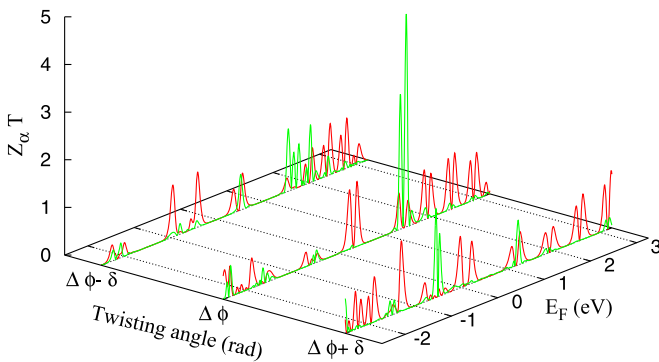


FIG. 11. Charge and spin thermoelectric FOMs as a function of Fermi energy at different twisting angle $\Delta\phi$, represented by the red and green colors, respectively for LRH helix. The considered $\Delta\phi$ values are $\Delta\phi - \delta, \Delta\phi$, and $\Delta\phi + \delta$. Here $\Delta\phi = 5\pi/9$ and $\delta \sim 0.087$ rad, which is equivalent to 5° . All the other parameters are identical with Fig. 2.

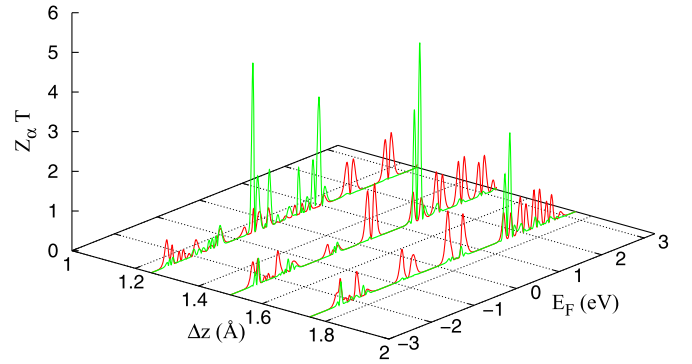


FIG. 12. Charge and spin thermoelectric FOMs as a function of Fermi energy at different stacking distances as shown by the red and green colors, respectively for LRH helix. The considered Δz values are $\Delta z = 1.25, 1.5$ (included for comparison), and 1.75 Å. All the other parameters are identical with Fig. 2.

maximum spin FOM reaches approximately 1.3 for the case $\Delta\phi - \delta$, and it is around 1.9 for $\Delta\phi + \delta$. Additionally, the charge FOM remains consistently above unity in both cases. This demonstrates that an advantageous outcome can still be achieved even with slight to moderate adjustments in $\Delta\phi$.

3. Role of Δz

The stacking distance Δz significantly influences the geometric structure of the helix, and as a result, the FOM should be sensitive to its variations. A smaller value of Δz indicates a tendency towards long-range hopping, while a larger value of Δz suggests a preference for short-range hopping. Previously, Δz was fixed at 1.5 Å. Here we consider two different stacking distances, namely $\Delta z = 1.25$ and 1.75 Å. The results are shown in Fig. 12 including the result for the previously chosen value of Δz for comparison. We see that the spin FOM for both the cases are lower than the previous case but greater than unity. The maximum spin FOMs are about 4.3 and 2.7 for $\Delta z = 1.25$ and 1.75 Å, respectively. In general, the spin FOM is more favorable than the charge FOM for all the stacking distances considered in the present work.

4. Role of l_c

The decay constant l_c , significantly influences the pace at which successive higher order hopping integrals evolve. When l_c is set to a high value, the rate of decline in these successive higher order hopping integrals becomes comparatively slower than when l_c is set to a small value. As a result, the parameter l_c may play a critical role in shaping the TE response. To investigate the impact of varying l_c on TE behavior, we examine two distinct values: 0.8 and 1 Å. Figure 13 displays the corresponding results. Additionally, we include the TE results for $l_c = 0.9$ Å to aid comparison. It appears that the TE response for spin FOM is quite good for the considered values of l_c within the Fermi energy window 1 to 2 eV. The maximum spin FOM are about 4.2 and 4.4 for $l_c = 0.8$ and 1 Å, respectively, which are comparable to that for $l_c = 0.9$ Å.

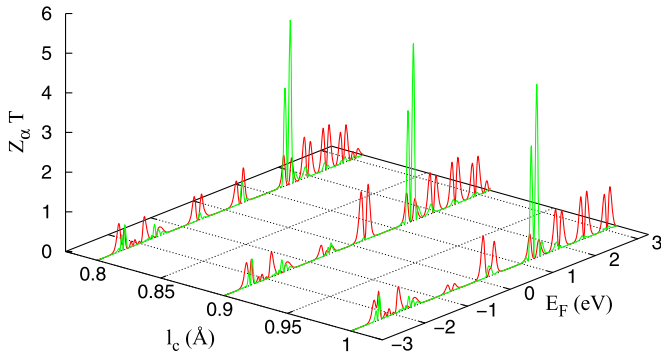


FIG. 13. Charge and spin thermoelectric FOMs as a function of Fermi energy at different values of the decay constant l_c as shown by the red and green colors, respectively for LRH helix. The considered l_c values are 0.8, 0.9 (included for comparison), and 1 Å. All the other parameters are identical with Fig. 2.

H. Size dependence

The impact of helix size on the TE response is investigated in Fig. 14. We choose the number of sites of the helix in such a way that it approximates an integer multiple of complete helical turns. For instance, to achieve a total of five complete turns in the LRH helix, we require 19 sites. In the current analysis, we approximate this as 20 sites for the LRH configuration to maintain a zero net magnetization for the AFH. Here, we also examine two additional helix sizes, characterized by 30 and 38 sites, corresponding to approximately eight and ten complete helical turns, respectively, in order to have a comparative analysis. The result for $N = 20$ is included here to provide a basis for comparison. Upon examining the plot, it becomes evident that there is a noticeable downward trend in the spin FOM as the system size increases. For $N = 20$, the maximum spin FOM was approximately 4.5. For larger helix sizes such as $N = 30$ and 38, the spin FOM decreases to approximately 3 and 1.9, respectively. Despite this decreasing trend, it is noteworthy that the spin FOM consistently exhibits a favorable response across all the selected helix sizes. The declining trend of spin FOM can be attributed to the fact that

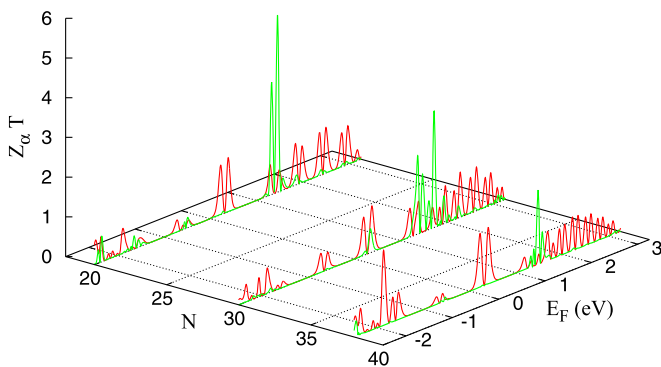


FIG. 14. Charge and spin thermoelectric FOMs as a function of Fermi energy for different helix sizes N as shown by the red and green colors, respectively for LRH helix. The considered number of sites in the helix are $N = 20$ (included for comparison), 30, and 38. All the other parameters are identical with Fig. 2.

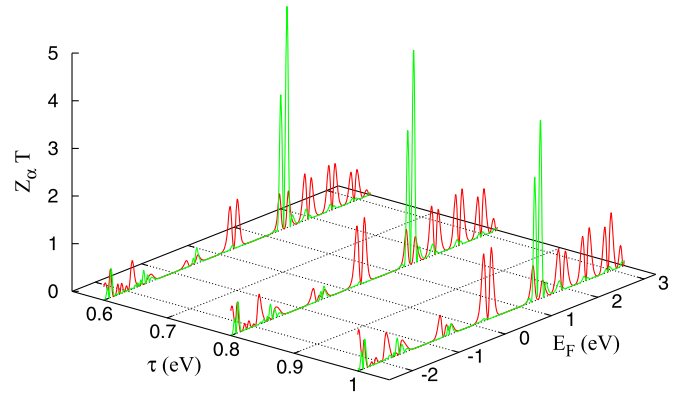


FIG. 15. Charge and spin thermoelectric FOMs as a function of Fermi energy for different coupling strengths τ as shown by the red and green colors, respectively for LRH helix. The chosen τ values are $\tau = 1, 0.8$ (included for comparison), and 0.6 eV. All the other parameters are identical with Fig. 2.

the increase in the helix size introduces more transmission peaks and reduces the degree of asymmetry about the center of the allowed band. What is particularly intriguing is that, while the charge FOM may not be as impressive as the spin FOM, it still consistently remains above unity for all the chosen helix sizes.

I. Effect of lead-helix coupling

In this section, we concentrate on the role of coupling between the helix and the contact leads. This coupling might have a significant effect on energy conversion efficiency as it directly controls the electron flow from the leads to the helix system. Strong coupling results in broader transmission peaks, whereas weaker coupling sharpens them [96,97]. Any sharp transmission peak introduces greater asymmetry in the transmission function, leading to a more favorable TE response. To illustrate this, we consider two different coupling strengths: $\tau_S = \tau_D = \tau = 1$ and 0.6 eV, in addition to the previously mentioned value of 0.8 eV for comparison. The results are depicted in Fig. 15. The maximum spin FOM is approximately 3.8, 4.5, and 4.7 for coupling strengths of 1, 0.8, and 0.6 eV, respectively. Hence, the spin FOM increases as we reduce the coupling strength, as explained earlier.

J. Effect of temperature

All the results discussed so far are at room temperature $T = 300$ K. To study the effect of temperature, we have plotted $Z_\alpha T$ as a function of Fermi energy for three other different temperatures, namely, $T = 150, 250,$ and 350 K, as shown in Fig. 16 for the LRH helix. The other parameters are kept fixed, as mentioned in Fig. 2. The spin ZT and the charge ZT are shown by the green and red colors, respectively. The temperature profile indicates that the maximum value of the spin FOM tends to increase with the increase in operating temperature. The maximum $Z_\alpha T$, in this case, is found to be around 4.7 at temperature 350 K.

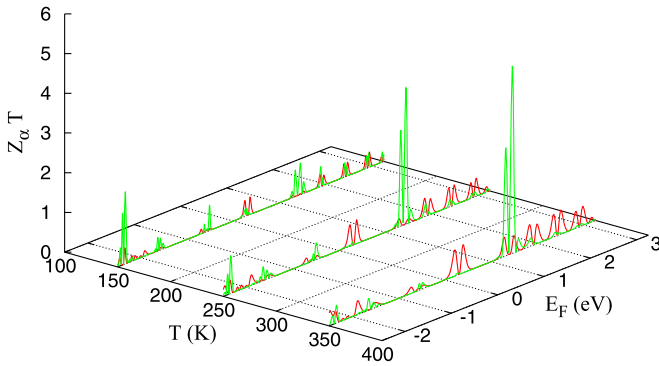


FIG. 16. Charge and spin thermoelectric FOMs as a function of Fermi energy at different temperatures as shown by the red and green colors, respectively for LRH helix. All the parameters are identical with Fig. 2.

Experimental feasibility of AF helix system

The experimental feasibility of antiferromagnetic (AF) helix structures has been successfully demonstrated in various materials, combining experimental techniques with theoretical studies. Notably, the metallic spiral antiferromagnet $\text{SrFeO}_{2.95}$ has been experimentally realized [98]. In polycrystalline samples of $\text{Lu}_{1-x}\text{Sc}_x\text{MnSi}$, long-range helical antiferromagnetic ordering has been observed at temperatures close to room temperature [99]. Recent studies using single-crystal neutron diffraction have reported an incommensurate antiferromagnetic spiral-like structure in EuNi_2As_2 [100], as well as in EuCo_2As_2 based on nuclear magnetic resonance results [101]. Additionally, helical antiferromagnetic ordering has been reported in a single crystal of $\text{EuNi}_{1.95}\text{As}_2$ [102]. Spin-canted antiferromagnetism with helical topology has been observed in $[\text{M}(\text{mtpo})_2(\text{H}_2\text{O})]_n$ systems, where M represents Co^{2+} or Ni^{2+} , exhibiting canted antiferromagnetic ordering [103]. Furthermore, a recent work has discussed the possibility of curvilinear one-dimensional antiferromagnets [104]. In this work, the authors showed that even an intrinsically achiral one-dimensional curvilinear antiferromagnet can exhibit chiral helimagnetic behavior with geometrically tunable Dzyaloshinskii-Moriya interaction and Néel vector orientation. These experimental demonstrations and many others highlight the diverse range of materials where AF helix structures have been observed, providing strong evidence for their existence.

Taking into account various instances of antiferromagnetic helical systems, we have confidence that our proposed AF helix system can be engineered utilizing contemporary

technology and an appropriate laboratory configuration to study the spin TE response.

It is worth noting that the experimental references mentioned above all involve heavy magnetic elements, which may raise the question of whether the tight-binding Hamiltonian presented in Eq. (2) can accurately describe our helix systems. However, the theoretical study by Takahashi and Igarashi [105] provides us with reassurance that Eq. (2) is a suitable description. In their work, they also utilized a similar tight-binding Hamiltonian to describe materials such as La_2CuO_4 and $\text{Sr}_2\text{CuO}_2\text{Cl}_2$. Additionally, there are several other references [106,107] where tight-binding Hamiltonians have been employed to model heavy magnetic elements of this type. Therefore we can confidently use the tight-binding Hamiltonian in Eq. (2) to describe our helix systems, despite the heavy magnetic elements present.

IV. CONCLUSIONS

In this present work, we have proposed a scheme to achieve a favorable spin TE response in a typical helical geometry with a spin configuration of antiferromagnetic texture. We have considered both the short-range and long-range hopping scenarios. We have considered the spin-dependent scattering phenomena and also a transverse electric field to study thermoelectric physics in the helical system. In the absence of electric field or helicity, spin-dependent phenomena is no longer observed. We have used the NEGF formalism following the Landauer-Buttiker prescription to study the thermoelectric phenomena. Both the charge and spin TE responses have been studied. For a precise estimation of the TE *figure of merit*, we have computed the phonon contribution to the total thermal conductance. We have achieved a highly favorable spin TE response compared to the charge counterpart at room temperature for both the SRH and LRH molecules. The role of spin-dependent scattering factor, electric field, helix characteristics, TB parameters, temperature, etc., have also been examined on the spin TE behavior. From our extensive numerical analysis, we have clearly seen that the favorable thermoelectric response persists over a broad range of physical parameters and under different input conditions, which proves the robustness of our analysis.

To the best of our concern, spin-dependent TE phenomena in antiferromagnetic helix have not been studied so far in the literature. All the results have been explained with proper physical arguments, that might be helpful for the readers along this line. Our proposition may provide a new route of achieving efficient energy conversion using similar kinds of other fascinating antiferromagnetic systems as well.

[1] G. J. Snyder and E. S. Toberer, Complex thermoelectric materials, *Nat. Mater.* **7**, 105 (2008).
 [2] J. He and T. M. Tritt, Advances in thermoelectric materials research: Looking back and moving forward, *Science* **357**, eaak9997 (2017).
 [3] L. D. Hicks and M. S. Dresselhaus, Effect of quantum-well structures on the thermoelectric figure of merit, *Phys. Rev. B* **47**, 12727 (1993).

[4] A. Majumdar, Thermoelectricity in semiconductor nanostructures, *Science* **303**, 777 (2004).
 [5] B. Kubala, J. König, and J. Pekola, Violation of the Wiedemann-Franz law in a single-electron transistor, *Phys. Rev. Lett.* **100**, 066801 (2008).
 [6] L. D. Hicks and M. S. Dresselhaus, Thermoelectric figure of merit of a one-dimensional conductor, *Phys. Rev. B* **47**, 16631 (1993).

- [7] Y. Dubi and M. Di Ventra, Thermospin effects in a quantum dot connected to ferromagnetic leads, *Phys. Rev. B* **79**, 081302 (2009).
- [8] R. Świrkowicz, M. Wierzbicki, and J. Barnaś, Thermoelectric effects in transport through quantum dots attached to ferromagnetic leads with noncollinear magnetic moments, *Phys. Rev. B* **80**, 195409 (2009).
- [9] D. M.-T. Kuo and Y.-C. Chang, Thermoelectric and thermal rectification properties of quantum dot junctions, *Phys. Rev. B* **81**, 205321 (2010).
- [10] M. Wierzbicki and R. Świrkowicz, Influence of interference effects on thermoelectric properties of double quantum dots, *Phys. Rev. B* **84**, 075410 (2011).
- [11] P. Trocha and J. Barnaś, Large enhancement of thermoelectric effects in a double quantum dot system due to interference and Coulomb correlation phenomena, *Phys. Rev. B* **85**, 085408 (2012).
- [12] J. E. Cornett and O. Rabin, Universal scaling relations for the thermoelectric power factor of semiconducting nanostructures, *Phys. Rev. B* **84**, 205410 (2011).
- [13] V. Balachandran, R. Bosisio, and G. Benenti, Validity of the Wiedemann-Franz law in small molecular wires, *Phys. Rev. B* **86**, 035433 (2012).
- [14] Y. Qi, Z. Wang, M. Zhang, F. Yang, and X. Wang, Thermoelectric devices based on one-dimensional nanostructures, *J. Mater. Chem. A* **1**, 6110 (2013).
- [15] I.-J. Chen, A. Burke, A. Svilans, H. Linke, and C. Thelander, Thermoelectric power factor limit of a 1D nanowire, *Phys. Rev. Lett.* **120**, 177703 (2018).
- [16] Y. Xu, R.-L. Chu, and C. Zhang, Anisotropic weyl fermions from the quasiparticle excitation spectrum of a 3D Fulde-Ferrell superfluid, *Phys. Rev. Lett.* **112**, 136402 (2014).
- [17] N. Xu, Y. Xu, and J. Zhu, Topological insulators for thermoelectrics, *npj Quantum Mater.* **2**, 51 (2017).
- [18] D. Segal, Thermoelectric effect in molecular junctions: A tool for revealing transport mechanisms, *Phys. Rev. B* **72**, 165426 (2005).
- [19] P. Reddy, S.-Y. Jang, R. A. Segalman, and A. Majumdar, Thermoelectricity in molecular junctions, *Science* **315**, 1568 (2007).
- [20] D. Nozaki, H. Sevinçli, W. Li, R. Gutiérrez, and G. Cuniberti, Engineering the figure of merit and thermopower in single-molecule devices connected to semiconducting electrodes, *Phys. Rev. B* **81**, 235406 (2010).
- [21] Y. Dubi and M. Di Ventra, Colloquium: Heat flow and thermoelectricity in atomic and molecular junctions, *Rev. Mod. Phys.* **83**, 131 (2011).
- [22] E. Maciá, Thermoelectric power and electrical conductance of dna based molecular junctions, *Nanotechnology* **16**, S254 (2005).
- [23] E. Maciá, Dna-based thermoelectric devices: A theoretical perspective, *Phys. Rev. B* **75**, 035130 (2007).
- [24] E. Maciá, Codon thermoelectric signature in molecular junctions, *Phys. Rev. B* **82**, 045431 (2010).
- [25] Y.-J. Dong, X.-F. Wang, Y.-S. Liu, and X.-M. Wu, Length enhancement of thermoelectric effects in DNA duplex chains due to quantum interferences, *Org. Electron.* **26**, 176 (2015).
- [26] Y. Li, L. Xiang, J. L. Palma, Y. Asai, and N. Tao, Thermoelectric effect and its dependence on molecular length and sequence in single DNA molecules, *Nat. Commun.* **7**, 11294 (2016).
- [27] D. E. Nikonov, G. I. Bourianoff, and P. A. Gargini, Power dissipation in spintronic devices out of thermodynamic equilibrium, *J. Supercond. Novel Magn.* **19**, 497 (2006).
- [28] M. Johnson and R. H. Silsbee, Interfacial charge-spin coupling: Injection and detection of spin magnetization in metals, *Phys. Rev. Lett.* **55**, 1790 (1985).
- [29] M. N. Baibich, J. M. Broto, A. Fert, F. Nguyen Van Dau, F. Petroff, P. Etienne, G. Creuzet, A. Friederich, and J. Chazelas, Giant magnetoresistance of (001)Fe/(001)Cr magnetic superlattices, *Phys. Rev. Lett.* **61**, 2472 (1988).
- [30] I. Žutić, J. Fabian, and S. Das Sarma, Spintronics: Fundamentals and applications, *Rev. Mod. Phys.* **76**, 323 (2004).
- [31] J. P. Lu, J. B. Yau, S. P. Shukla, M. Shayegan, L. Wissinger, U. Rössler, and R. Winkler, Tunable spin-splitting and spin-resolved ballistic transport in gaas/algaas two-dimensional holes, *Phys. Rev. Lett.* **81**, 1282 (1998).
- [32] J. Zheng, F. Chi, and Y. Guo, Large spin figure of merit in a double quantum dot coupled to noncollinear ferromagnetic electrodes, *J. Phys.: Condens. Matter* **24**, 265301 (2012).
- [33] H. J. Goldsmid *et al.*, *Introduction to Thermoelectricity* (Springer, 2010), Vol. 121.
- [34] M. Johnson and R. H. Silsbee, Thermodynamic analysis of interfacial transport and of the thermomagnetolectric system, *Phys. Rev. B* **35**, 4959 (1987).
- [35] G. E. W. Bauer, E. Saitoh, and B. J. van Wees, Spin caloritronics, *Nat. Mater.* **11**, 391 (2012).
- [36] E. Saitoh, M. Ueda, H. Miyajima, and G. Tatara, Conversion of spin current into charge current at room temperature: Inverse spin-hall effect, *Appl. Phys. Lett.* **88**, 182509 (2006).
- [37] S. O. Valenzuela and M. Tinkham, Direct electronic measurement of the spin hall effect, *Nature (London)* **442**, 176 (2006).
- [38] T. Kimura, Y. Otani, T. Sato, S. Takahashi, and S. Maekawa, Room-temperature reversible spin hall effect, *Phys. Rev. Lett.* **98**, 156601 (2007).
- [39] H. Adachi, K. ichi Uchida, E. Saitoh, and S. Maekawa, Theory of the spin seebeck effect, *Rep. Prog. Phys.* **76**, 036501 (2013).
- [40] A. Kirihara, K.-I. Uchida, Y. Kajiwara, M. Ishida, Y. Nakamura, T. Manako, E. Saitoh, and S. Yoroza, Spin-current-driven thermoelectric coating, *Nat. Mater.* **11**, 686 (2012).
- [41] Ken-ichi Uchida, A. Kirihara, M. Ishida, R. Takahashi, and E. Saitoh, Local spin-seebeck effect enabling two-dimensional position sensing, *Jpn. J. Appl. Phys.* **50**, 120211 (2011).
- [42] Ken-ichi Uchida, T. Nonaka, T. Yoshino, T. Kikkawa, D. Kikuchi, and E. Saitoh, Enhancement of spin-seebeck voltage by spin-hall thermopile, *Appl. Phys. Express* **5**, 093001 (2012).
- [43] X.-F. Ouyang, Z.-Y. Song, and Y.-Z. Zhang, Fully spin-polarized current in gated bilayer silicene, *Phys. Rev. B* **98**, 075435 (2018).
- [44] J. A. Gauthier, M. Fields, M. Bajdich, L. D. Chen, R. B. Sandberg, K. Chan, and J. K. Nørskov, Facile electron transfer to Co₂ during adsorption at the metal solution interface, *J. Phys. Chem. C* **123**, 29278 (2019).
- [45] K. Tsukagoshi, B. W. Alphenaar, and H. Ago, Coherent transport of electron spin in a ferromagnetically contacted carbon nanotube, *Nature (London)* **401**, 572 (1999).
- [46] S. Kamboj, D. K. Roy, S. Roy, R. R. Chowdhury, P. Mandal, M. Kabir, and G. Sheet, Temperature dependent transport spin-

- polarization in the low curie temperature complex itinerant ferromagnet $\text{EuTi}_{1-x}\text{Nb}_x\text{O}_3$, *J. Phys.: Condens. Matter* **31**, 415601 (2019).
- [47] E. I. Rashba, Theory of electrical spin injection: Tunnel contacts as a solution of the conductivity mismatch problem, *Phys. Rev. B* **62**, R16267 (2000).
- [48] K. Premasiri, S. K. Radha, S. Sucharitakul, U. R. Kumar, R. Sankar, F.-C. Chou, Y.-T. Chen, and X. P. Gao, Tuning rashba spin-orbit coupling in gated multilayer inSe, *Nano Lett.* **18**, 4403 (2018).
- [49] S. Ganguly and S. K. Maiti, Selective spin transmission through a driven quantum system: A new prescription, *J. Appl. Phys.* **129**, 123902 (2021).
- [50] B. K. Nikolić, L. P. Žárbo, and S. Souma, Imaging mesoscopic spin hall flow: Spatial distribution of local spin currents and spin densities in and out of multiterminal spin-orbit coupled semiconductor nanostructures, *Phys. Rev. B* **73**, 075303 (2006).
- [51] P. Földi, O. Kálmán, M. G. Benedict, and F. M. Peeters, Quantum rings as electron spin beam splitters, *Phys. Rev. B* **73**, 155325 (2006).
- [52] M. Dey, S. K. Maiti, S. Sil, and S. Karmakar, Spin-orbit interaction induced spin selective transmission through a multi-terminal mesoscopic ring, *J. Appl. Phys.* **114**, 164318 (2013).
- [53] Y.-H. Su, S.-H. Chen, C. D. Hu, and C.-R. Chang, Competition between spin-orbit interaction and exchange coupling within a honeycomb lattice ribbon, *J. Phys. D* **49**, 015305 (2016).
- [54] V. Baltz, A. Manchon, M. Tsoi, T. Moriyama, T. Ono, and Y. Tserkovnyak, Antiferromagnetic spintronics, *Rev. Mod. Phys.* **90**, 015005 (2018).
- [55] T. Jungwirth, J. Sinova, A. Manchon, X. Marti, J. Wunderlich, and C. Felser, The multiple directions of antiferromagnetic spintronics, *Nat. Phys.* **14**, 200 (2018).
- [56] M. B. Jungfleisch, W. Zhang, and A. Hoffmann, Perspectives of antiferromagnetic spintronics, *Phys. Lett. A* **382**, 865 (2018).
- [57] P. Y. Artemchuk, O. Sulymenko, S. Louis, J. Li, R. Khymyn, E. Bankowski, T. Meitzler, V. Tyberkevych, A. Slavin, and O. Prokopenko, Terahertz frequency spectrum analysis with a nanoscale antiferromagnetic tunnel junction, *J. Appl. Phys.* **127**, 063905 (2020).
- [58] P. Wadley, B. Howells, J. Železný, C. Andrews, V. Hills, R. P. Campion, V. Novák, K. Olejník, F. Maccherozzi, S. S. Dhesi, S. Y. Martin, T. Wagner, J. Wunderlich, F. Freimuth, Y. Mokrousov, J. Kuneš, J. S. Chauhan, M. J. Grzybowski, A. W. Rushforth, K. W. Edmonds *et al.*, Electrical switching of an antiferromagnet, *Science* **351**, 587 (2016).
- [59] P. Němec, M. Fiebig, T. Kampfrath, and A. V. Kimel, Antiferromagnetic opto-spintronics, *Nat. Phys.* **14**, 229 (2018).
- [60] T. Kosub, M. Kopte, R. Hühne, P. Appel, B. Shields, P. Maletinsky, R. Hübner, M. O. Liedke, J. Fassbender, O. G. Schmidt, and D. Makarov, Purely antiferromagnetic magnetoelectric random access memory, *Nat. Commun.* **8**, 13985 (2017).
- [61] D. D. Gupta and S. K. Maiti, Can a sample having zero net magnetization produce polarized spin current? *J. Phys.: Condens. Matter* **32**, 505803 (2020).
- [62] B. Göhler, V. Hamelbeck, T. Z. Markus, M. Kettner, G. F. Hanne, Z. Vager, R. Naaman, and H. Zacharias, Spin selectivity in electron transmission through self-assembled monolayers of double-stranded DNA, *Science* **331**, 894 (2011).
- [63] A.-M. Guo and Q. F. Sun, Spin-selective transport of electrons in DNA double helix, *Phys. Rev. Lett.* **108**, 218102 (2012).
- [64] A.-M. Guo and Q.-F. Sun, Spin-dependent electron transport in protein-like single-helical molecules, *Proc. Natl. Acad. Sci. USA* **111**, 11658 (2014).
- [65] D. Mishra, T. Z. Markus, R. Naaman, M. Kettner, B. Göhler, H. Zacharias, N. Friedman, M. Sheves, and C. Fontanesi, Spin-dependent electron transmission through bacteriorhodopsin embedded in purple membrane, *Proc. Natl. Acad. Sci. USA* **110**, 14872 (2013).
- [66] R. Gutierrez, E. Díaz, R. Naaman, and G. Cuniberti, Spin-selective transport through helical molecular systems, *Phys. Rev. B* **85**, 081404(R) (2012).
- [67] T.-R. Pan, A.-M. Guo, and Q.-F. Sun, Effect of gate voltage on spin transport along α -helical protein, *Phys. Rev. B* **92**, 115418 (2015).
- [68] A.-M. Guo and Q.-F. Sun, Topological states and quantized current in helical organic molecules, *Phys. Rev. B* **95**, 155411 (2017).
- [69] S. Datta, *Electronic Transport in Mesoscopic Systems* (Cambridge University Press, 1997)
- [70] D. S. Fisher and P. A. Lee, Relation between conductivity and transmission matrix, *Phys. Rev. B* **23**, 6851 (1981).
- [71] M. Di Ventra, Electrical transport in nanoscale systems, *Electrical Transport in Nanoscale Systems* (2008).
- [72] B. K. Nikolic and P. B. Allen, Quantum transport in ballistic conductors: evolution from conductance quantization to resonant tunnelling, *J. Phys.: Condens. Matter* **12**, 9629 (2000).
- [73] A. A. Shokri, M. Mardaani, and K. Esfarjani, Spin filtering and spin diode devices in quantum wire systems, *Phys. E* **27**, 325 (2005).
- [74] A. A. Shokri and M. Mardaani, Spin-flip effect on electrical transport in magnetic quantum wire systems, *Solid State Commun.* **137**, 53 (2006).
- [75] M. Dey, S. K. Maiti, and S. Karmakar, Magnetic quantum wire as a spin filter: An exact study, *Phys. Lett. A* **374**, 1522 (2010).
- [76] M. Patra and S. K. Maiti, Externally controlled high degree of spin polarization and spin inversion in a conducting junction: Two new approaches, *Sci. Rep.* **7**, 14313 (2017).
- [77] S. Sarkar and S. K. Maiti, Spin-selective transmission through a single-stranded magnetic helix, *Phys. Rev. B* **100**, 205402 (2019).
- [78] E. Zerah-Harush and Y. Dubi, Enhanced thermoelectric performance of hybrid nanoparticle-single-molecule junctions, *Phys. Rev. Appl.* **3**, 064017 (2015).
- [79] C. M. Finch, V. M. García-Suárez, and C. J. Lambert, Giant thermopower and figure of merit in single-molecule devices, *Phys. Rev. B* **79**, 033405 (2009).
- [80] M. Shirdel-Havar and R. Farghadan, Spin caloritronics in spin semiconducting armchair graphene nanoribbons, *Phys. Rev. B* **97**, 235421 (2018).
- [81] F. Ildarabadi and R. Farghadan, Spin-thermoelectric transport in nonuniform strained zigzag graphene nanoribbons, *Phys. Rev. B* **103**, 115424 (2021).
- [82] T. M. Tritt, Thermoelectric phenomena, materials, and applications, *Annu. Rev. Mater. Res.* **41**, 433 (2011).

- [83] W. Zhang, T. S. Fisher, and N. Mingo, The atomistic green's function method: An efficient simulation approach for nanoscale phonon transport, *Numer. Heat Transfer, Part B* **51**, 333 (2007).
- [84] P. E. Hopkins and J. R. Serrano, Phonon localization and thermal rectification in asymmetric harmonic chains using a nonequilibrium green's function formalism, *Phys. Rev. B* **80**, 201408(R) (2009).
- [85] P. E. Hopkins, P. M. Norris, M. S. Tsegaye, and A. W. Ghosh, Extracting phonon thermal conductance across atomic junctions: Nonequilibrium Green's function approach compared to semiclassical methods, *J. Appl. Phys.* **106**, 063503 (2009).
- [86] K. Mondal, S. Ganguly, and S. K. Maiti, Possible route to efficient thermoelectric applications in a driven fractal network, *Sci. Rep.* **11**, 17049 (2021).
- [87] W. A. Harrison, *Electronic Structure and the Properties of Solids: The Physics of the Chemical Bond* (Freeman, 1980).
- [88] C. Kittel, *Introduction to Solid State Physics* (Wiley, 1956).
- [89] S. Aubry and G. André, Analyticity breaking and anderson localization in incommensurate lattices, *Ann. Isr. Phys. Soc.* **3**, 133 (1980).
- [90] R. J. Bursill, C. Castleton, and W. Barford, Optimal parametrisation of the Pariser-Parr-pople model for benzene and biphenyl, *Chem. Phys. Lett.* **294**, 305 (1998).
- [91] S. Ganeshan, K. Sun, and S. Das Sarma, Topological zero-energy modes in gapless commensurate Aubry-André-Harper models, *Phys. Rev. Lett.* **110**, 180403 (2013).
- [92] G. D. Mahan and J. O. Sofo, The best thermoelectric, *Proc. Natl. Acad. Sci.* **93**, 7436 (1996).
- [93] J. M. Cullen and J. M. Allwood, Theoretical efficiency limits for energy conversion devices, *Energy* **35**, 2059 (2010).
- [94] J. R. Neighbours and G. A. Alers, Elastic constants of silver and gold, *Phys. Rev.* **111**, 707 (1958).
- [95] J. C. W. Heseltine, D. W. Elliott, and O. B. Wilson, Elastic constants of single-crystal benzene, *J. Chem. Phys.* **40**, 2584 (1964).
- [96] E. Maciá, F. Triozon, and S. Roche, Contact-dependent effects and tunneling currents in DNA molecules, *Phys. Rev. B* **71**, 113106 (2005).
- [97] K. Lambropoulos and C. Simserides, Spectral and transmission properties of periodic 1D tight-binding lattices with a generic unit cell: An analysis within the transfer matrix approach, *J. Phys. Commun.* **2**, 035013 (2018).
- [98] R. Dahiya, A. Agarwal, S. Sanghi, A. Hooda, and P. Godara, Structural, magnetic and dielectric properties of Sr and V doped BiFeO₃ multiferroics, *J. Magn. Magn. Mater.* **385**, 175 (2015).
- [99] R. J. Goetsch, V. K. Anand, and D. C. Johnston, Helical antiferromagnetic ordering in Lu_{1-x}Sc_xMnSi, *Phys. Rev. B* **90**, 064415 (2014).
- [100] W. T. Jin, N. Qureshi, Z. Bukowski, Y. Xiao, S. Nandi, M. Babij, Z. Fu, Y. Su, and T. Brückel, Spiral magnetic ordering of the Eu moments in EuNi₂As₂, *Phys. Rev. B* **99**, 014425 (2019).
- [101] Q.-P. Ding, N. Higa, N. S. Sangeetha, D. C. Johnston, and Y. Furukawa, NMR determination of an incommensurate helical antiferromagnetic structure in EuCo₂As₂, *Phys. Rev. B* **95**, 184404 (2017).
- [102] N. S. Sangeetha, V. Smetana, A.-V. Mudring, and D. C. Johnston, Helical antiferromagnetic ordering in EuNi_{1.95}As₂ single crystals, *Phys. Rev. B* **100**, 094438 (2019).
- [103] Q.-P. Lin, J. Zhang, X.-Y. Cao, Y.-G. Yao, Z.-J. Li, L. Zhang, and Z.-F. Zhou, Canted antiferromagnetic behaviours in isostructural Co(ii) and Ni(ii) frameworks with helical 1vt topology, *CrystEngComm* **12**, 2938 (2010).
- [104] O. V. Pylypovskyi, D. Y. Kononenko, K. V. Yershov, U. K. Röbller, A. V. Tomilo, J. Fassbender, J. van den Brink, D. Makarov, and D. D. Sheka, Curvilinear one-dimensional antiferromagnets, *Nano Lett.* **20**, 8157 (2020).
- [105] M. Takahashi and J. I. Igarashi, Local approach to electronic excitations in the insulating copper oxides La₂CuO₄ and Sr₂CuO₂Cl₂, *Phys. Rev. B* **59**, 7373 (1999).
- [106] M. J. DeWeert, D. A. Papaconstantopoulos, and W. E. Pickett, Tight-binding hamiltonians for high-temperature superconductors and applications to coherent-potential-approximation calculations of the electronic properties of La_{2-x}Ba_xCuO_{4-y}, *Phys. Rev. B* **39**, 4235 (1989).
- [107] C. Cao, P. J. Hirschfeld, and H.-P. Cheng, Proximity of antiferromagnetism and superconductivity in LaFeAsO_{1-x}F_x: Effective hamiltonian from *ab initio* studies, *Phys. Rev. B* **77**, 220506(R) (2008).